UFKW propagation in the dissipative thermosphere

Jeffrey M. Forbes[1], **Xiaoli Zhang**[1], **Scott E. Palo**[1]

[1]Ann and H.J. Smead Department of Aerospace Engineering Sciences, University of Colorado, Boulder, CO

Key Points:

- UFKW with periods less than about 4 days can effectively penetrate above 100 km altitude.
- Dissipation broadens UFKW latitude structures with increasing height and lengthens vertical wavelengths with increasing latitude.
- Ion drag dampens UFKW amplitudes with increasing efficiency at higher solar activity levels.

Corresponding author: Jeffrey M. Forbes, `forbes@colorado.edu`

Abstract

"Ultra-fast" Kelvin waves (UFKWs) serve as a mechanism for coupling the tropical troposphere with the mesosphere, thermosphere and ionosphere. Herein, solutions to the linearized wave equations in a dissipative thermosphere in the form of "Hough Mode Extensions (HMEs)" are employed to better understand the vertical propagation of the subset of these waves that most effectively penetrate into the thermosphere above about 100 km altitude; namely, UFKWs with periods $\lesssim$ 4d, vertical wavelengths (λ_z) $\gtrsim$ 30 km, and zonal wavenumber $s = -1$. Molecular dissipation is found to broaden latitude structures of UFKWs with increasing height while their vertical wavelengths (λ_z) increase with latitude. Collisions with ions fixed to Earth's magnetic field ("ion drag") are found to dampen UFKW amplitudes, increasingly so as the densities of those ions increase with increased solar flux. The direct effect of ion drag is to decelerate the zonal wind. This leads to suppression of vertical velocity and the velocity divergence, and related terms in the continuity and thermal energy equations, respectively, that lead to diminished perturbation temperature and density responses. Access is provided to the UFKW HMEs analyzed here in tabular and graphical form, and potential uses for future scientific studies are noted.

1 Plain Language Summary

In earth's atmosphere, Kelvin waves (KWs) are eastward-propagating oscillations with periods of days to weeks that are centered on the equator and confined to low latitudes. They are forced by the spatial-temporal variability of the heat of condensation ("latent heating") that is released when rising moist air forms rain droplets, mainly in the tropics. As with many atmospheric waves, they propagate vertically and grow exponentially with height in concert with the decrease in atmospheric density and pressure. The KWs that survive the trip from near the surface to about 100 km altitude are called 'ultra-fast" Kelvin waves, or UFKWs. Just above 100 km, they reach maximum amplitudes where their exponential growth is curtailed by the viscosity of this part of the atmosphere. Here they interact with ionized particles (the ionosphere) and generate electric fields that ultimately drive ionospheric variability at higher altitudes (> 200 km), thus presenting an element of "space weather" to navigation and communications systems. In this paper we model a set of UFKWs to better understand how their amplitudes, vertical and latitudinal structures change as they propagate above 100 km, and in so doing advance our knowledge of the physical processes underpinning near-earth space weather.

2 Introduction

In the classical theory of waves in a rotating, horizontally-stratified atmosphere without dissipation, the linearized wave equations are separable in height and latitude, giving rise to an eigenfunction-eigenvalue problem wherein the eigenfunctions(eigenvalues) of Laplace's tidal equation (LTE) define the waves' latitudinal(vertical) structures (e.g., Chapman and Lindzen, 1970; Longuet-Higgins, 1968; Volland, 1988). When the eigenvalues are plotted versus wave frequency, both gravity-type ("Class I") and rotational ("Class II") waves can be identified, both eastward- and westward-propagating, with positive and negative eigenvalues. Positive eigenvalues are generally associated with vertical propagation, while negative eigenvalues are generally associated with vertically-trapped or evanescent solutions. Kelvin waves are the first symmetric modes of the eastward-propagating Class I oscillations. They are characterized by Gaussian-shaped horizontal structures centered on the equator for zonal winds, temperature, vertical velocity, density, and pressure, and comparatively small meridional winds that are antisymmetric about the equator. Kelvin waves are thought to be primarily generated by latent heating associated with tropical convection. This paper is concerned with the subset of Kelvin waves with high enough phase speeds to survive filtering and dissipation in the mesosphere and stratosphere, and with large enough amplitudes to measurably impact the dynamics and electrodynamics of the thermosphere and ionosphere; these are referred to as "ultra-fast Kelvin waves" (UFKW, Salby, 1984). Based on measurements that reflect UFKW activity in the vicinity of 100 km as well as the F-region ionosphere (e.g., Chang et al., 2010; Forbes et al., 2009; Gu et al., 2014; Liu et al., 2015; and references therein), and theoretical constraints imposed later in this paper, in practice this means UFKW periods between about 2 and 5 days (hereafter 2d and 5d) and zonal wavenumber $s = -1$, where $s < 0$ implies eastward propagation (see below).

UFKWs and solar tides are similar in many respects, and in fact the same mathematical formulation can be adopted for both. The expression

$$A(z,\theta)cos(\omega t + s\lambda - \phi(z,\theta)) \qquad (1)$$

represents a global-scale atmospheric oscillation in any atmospheric variable (e.g., temperature, wind speed, etc.), where $A(z,\theta)$ is its amplitude; z is altitude; θ is latitude; ω is wave frequency; t is Universal Time, UT; s is the zonal wavenumber; λ is longitude; and $\phi(z,\theta)$ is its phase (UT of amplitude maximum at $\lambda = 0$, or longitude of maximum at UT = 0). In this notation $s < 0 (s > 0)$ implies eastward(westward) propagation. Expression (1) applies to tides if $\omega = n\Omega$ where $\Omega = 2\pi$ d^{-1} and integer $n = 1, 2, 3$ refers to diurnal, semidiurnal and terdiurnal oscillations, respectively. Expression (1) applies to UFKWs if n is replaced by non-integer $\delta = 1/\tau$ in the definition of ω, where τ is the wave period (d); for instance, $\delta = 0.5$ corresponds to a 2d UFKW, and $\delta = 0.25$ corresponds to a 4d UFKW.

Observations of solar tides and UFKWs that identify their zonal wavenumbers are practically absent within the 110 km to 300 km height regime where these waves undergo dissipation, maximize in amplitude, and approach asymptotic values due to increasingly efficient molecular diffusion of heat and momentum. Most of what we know is inferred from modeling, which has been mainly devoted to solar tides. In this regard, a methodology has been developed to "extend" the Hough modes of classical tidal theory into the dissipative thermosphere. This methodology involves solving the linearized tidal equations for an oscillation of a given frequency and zonal wavenumber in the thermosphere where dissipation in the form of molecular diffusion and anisotropic ion drag dominate the solutions. And, in order for HMEs to serve as basis functions that are universally applicable, the background atmospheric state is assumed to be horizontally-stratified (i.e., latitude-independent). This also implies zero mean winds. These constraints are consistent with the assumptions leading to the existence of Hough modes in an atmosphere without dissipation. Thermosphere dissipation combined with planetary rotation renders the solutions inseparable; that is, the horizontal structures are a function of height, or equivalently, the vertical structures are a function of latitude. The inseparability also requires a numerical solution. The resulting height-latitude structures for each Hough Mode are referred to as 'Hough Mode Extensions' (HMEs; Lindzen et al., 1977; Forbes and Hagan, 1982).

HMEs are global, extending pole to pole and from the source to 400 km altitude. They are forced with a heat source confined to the troposphere, and with latitude shape given by the corresponding classical Hough mode. The HMEs consist of perturbation zonal, meridional and vertical winds (U, V, W), temperature $(\Delta\mathrm{T})$, relative density $(\Delta\rho/\rho_0)$ and geopotential height $(\Delta\Phi_h)$ that possess internally self-consistent relative amplitude and phase relationships for any given HME. So, if the amplitude and phase of the perturbation wind field is known for a given HME at a single latitude and height, then all the fields $U, V, W, \Delta T, \Delta\rho/\rho_0, \Delta\Phi_h$ are known for all latitudes and all heights. This latter property of HMEs lends itself to the fitting of observational data. For example, Forbes et al. (1991) used HMEs to simultaneously fit SW2 winds and temperatures between 80 and 150 km, and by reconstruction arrived at a monthly climatological model of horizontal and vertical winds, temperatures and densities in this height region.

Svoboda et al. (2005) subsequently utilized HMEs to fit tidal wind components DE3, D0, DW1, and DW2 measured by the High Resolution Doppler Imager (HRDI) instrument on the Upper Atmosphere Research Satellite (UARS) at 95 km to similarly arrive at an internally-consistent global climatology of diurnal tidal temperatures, winds and densities in the 80 km to 120 km height region. Oberheide et al. (2010) conducted a similar tidal fitting/reconstruction investigation, except using monthly- and multi-year-mean tidal winds and temperatures between about 80 km and 120 km from the Thermosphere Ionosphere Mesosphere Energetics and Dynamics (TIMED) mission. This resulted in the Climatological Tidal Model of the Thermosphere (CTMT), consisting of monthly-mean diurnal and semidiurnal tidal winds, temperatures and perturbation densities extending from pole to pole and from 0 to 400 km altitude. Six diurnal and eight semidiurnal tidal components are included in the CTMT. Oberheide et al. (2009) and Häusler et al. (2012) fit DE3 HMEs to E-region observations, and demonstrated that the HME extensions at 400 km could capture the salient features of DE3 winds, temperatures and densities measured by the CHAMP satellite, which underscores the viability of HMEs to provide insights into coupling between ∼100 km and 400 km. More recently, HMEs have been fit to tidal winds and temperatures measured between 90 km and 110 km by the Ionospheric Connection (ICON) mission to then serve as global lower boundary conditions at 97 km for the Thermosphere Ionosphere Electrodynamics General Circulation Model-ICON (TIEGCM-ICON; Maute, 2017) (Forbes et al., 2015; see also Cullens et al., 2020). This enables self-consistent comparisons between E-region neutral dynamics and the plasma drifts and density redistributions in the F-region due to electric fields generated by dynamo action in the E-region.

Despite the similarities between solar tides and UFKWs noted previously, and the relevance of the latter to the dynamics and electrodynamics of the thermosphere-ionosphere, and to how these regions are influenced by the meteorology of the tropical troposphere, HMEs for UFKWs have never been computed. It is one objective of this paper to present computations of HMEs, and to analyze them to provide new insights into how UFKWs serve to vertically couple the lower and upper regions of the thermosphere and ionosphere.

Specific questions that we seek to answer are as follows: What are the fundamental characteristics of UFKW propagation in the dissipative thermosphere? How do these characteristics vary with wave period? How do UFKW and their propagation characteristics vary with level of solar activity? How are wind, temperature and density responses similar and different, and what is the underlying physics? A second objective of the present work is to document UFKW HMEs and to make them publicly available for future use by the research community. Towards these ends, the following section provides additional details on the computation of HMEs. Section 4 illustrates how UFKW penetration into the thermosphere varies with wave period and solar cycle; what changes in UFKW structure accompany viscous dissipation; the role of ion drag; and the solar cycle variability of $U, V, \Delta T$ and $\Delta\rho/\rho_0$ attributable to UFKWs. Conclusions are provided in Section 5.

3 Computation of UFKW HMEs

The model used to compute the HMEs is identical to that used by Forbes (1982) to investigate the vertical propagation of diurnal and semidiurnal tides into the thermosphere, except that specification of the background atmosphere and ionosphere through which the waves propagate has been modified. The model is steady-state, and solves the linearized momentum, thermal energy, hydrostatic, continuity and state equations for a specified forcing in the lower atmosphere. Complex solutions of the form $f' \sim \hat{f}expi(\omega t + s\lambda)$ are assumed for the three wind components u', v', w' (eastward, southward and vertical) and temperature, density and pressure perturbations T', ρ', p', on an assumed zonal- and diurnal-mean basic state, leading to consolidation into 4 second-order partial differential equations in $\hat{u}, \hat{v}, \hat{w}, \hat{T}$ with respect to height (z, 0 to approximately 400 km) and colatitude (θ, pole to pole). Perturbation relative densities and geopotential heights are calculated post-facto using the linearized continuity and state equations. A stretched vertical variable is implemented to enable different vertical resolutions in the lower boundary layer, middle atmosphere and thermosphere; tabulations in the Supporting Information (SI) (see below) are consequently based on sampling the output in increments of $\approx$ 4 km. See Forbes (1982) for additional details regarding stretched variable, boundary conditions, method of numerical solution, and so forth.

The molecular and thermal conductivities, and the formulation of ion drag coefficient used in the current work are those specified in Forbes (1982). His "moderate" profile of eddy diffusivity (ν_{eddy}) with maximum value of 50 m^{2}s-1 is also adopted here; UFKW simulations above 100 km are weakly dependent on this choice. As noted in the Introduction, the HME calculation assumes latitude-independent specifications of neutral atmosphere properties, ion drag and molecular dissipation. Herein the neutral atmosphere and ionosphere models used in Forbes (1982) are replaced by the NRLMSIS2.0 model (Emmert et al., 2020) and the analytic Chiu (1975) model, respectively. In NRMLMSIS2.0, the local time, longitude, and intra-annual variations are turned off, reducing the neutral density and temperature specifications for the HMEs to an annual- and diurnal-mean specification at the equator. The 10.7-cm solar flux unit (s.f.u.) values input into the model correspond to F10.7 = 75, 100, 125, 150, 175, and 200, which translate to exosphere temperatures of 753K, 853K, 943K, 1024K, 1096K, and 1159K. The corresponding temperature profiles are illustrated in Figure S1 of the SI.

For the ionospheric model, average profiles of electron density and ion drag coefficient for each level of solar activity were calculated that correspond to diurnal means at 0° longitude, and averaged between -30° and +30° latitude. This choice is consistent with the observed low-latitude extent of UFKWs near 100 km (e.g., Davis et al., 2012; Liu et al., 2015, 2019). The corresponding electron density profiles and ion drag coefficients for each level of solar activity are provided as Figures S2 and S3, respectively of the SI. Given the simple way that the background atmosphere and ionosphere are implemented in the model, use of the HMEs in scientific studies must keep these simplifications in mind.

Each HME is forced with a heat source confined to the troposphere, and with latitude shape given by the corresponding Hough mode. The heat source for each HME of a given period is arbitrarily normalized to yield an equatorial temperature amplitude of 10K at 98 km for F10.7 = 75. The same heat source is used for all HMEs of a given period, which means there can be very small differences from the 10K value at 98 km for other levels of solar activity. The phase at 98 km is also arbitrary, determined by the λ_z of the oscillation and by the arbitrarily chosen phase of heating (UT = 0 at 0° longitude). Amplitudes and phases (hereafter amps/phzs) of all other variables at all other heights and latitudes are consistent in a relative sense to this normalization, in keeping with the HME solutions described in the previous subsection.

Given that UFKW events are episodic, one might ask whether a steady-state HME is applicable to UFKWs in the actual thermosphere. Chang et al. (2010) used a GCM to investigate the ionosphere-thermosphere response to 3d UFKW lower-boundary forcing at 30 km lasting for 10 days. A maximum response (near to steady-state) in neutral density was achieved at 325 km within 4 days after forcing commenced, a steady-state was achieved after an additional 4 days, and the response continued at steady-state levels for an additional 6 days after the forcing was set to zero. Given that 3d UFKW events are observed to occur over 20 day periods (Liu et al., 2017), it is concluded that UFKWs are regularly long-lived enough to achieve quasi-steady-state conditions similar to those emulated in the HMEs.

As demonstrated in the following section, UFKWs with periods > 5d do not penetrate efficiently into the thermosphere due to their short λ_z (< 37 km) and relatively long periods which make them particularly susceptible to dissipation. The existing literature on UFKWs in the mesosphere/lower thermosphere (MLT), and on ionospheric coupling by UFKWs, are generally focused on the 3d UFKW. This is due in part to the fact that satellite-based data are generally required to get both zonal wavenumber and wave period, which restrict the Nyquist frequency to $0.5\mathrm{d}^{-1}$. However, there exists modeling (Pancheva et al., 2016; Forbes, Maute et al., 2020) and observational evidence (Gu et al., 2014; Forbes, He et al., 2020) that UFKW with periods in the 2d-3d range exist in the MLT. For these reasons, the present study is focused on UFKW with periods between 2d and 5d.

The HME data files described in the SI and accessible through Forbes et al. (2022) correspond to $s = -1$ UFKW simulations that extend from pole to pole and 0 to 400 km altitude, and correspond to wave periods between 2d and 5d at increments of 0.5d. In addition, by analogy with solar tides (e.g., Oberheide et al., 2009), UFKW are expected to exhibit measurable variability with respect to solar cycle, which warrants some quantification of those effects. Data files are therefore provided for F10.7 values of 75, 125, and 175 s.f.u. Height versus latitude (hereafter, htvslat) plots of U, V and T are also included in the SI for periods of 2,3,4 and 5d at these levels of solar activity.

Also included in the accessible data are files containing tabulations of various quantities related to solutions of LTE for each of the above HMEs. These include Hough functions that define the horizontal structures of heating used to force the HMEs, the corresponding U and V expansion functions, the eigenvalues of the UFKWs, and an estimate of the UFKW λ_z based on an isothermal atmosphere of 256K (i.e., H = 7.5 km and dH/dz = 0 in Equation (2) below). The eigenfunctions and eigenvalues were calculated using the same basic methodology as outlined in Chapman and Lindzen (1970), and were validated against a range of independently-determined values cited in , e.g., Flattery (1967) and Longuet-Higgins (1968).

4 Results

4.1 General UFKW HME characteristics

Figure 1 illustrates the htvslat structures of U, V and ΔT for the 3d UFKW. This 3d UFKW with $\Delta T = 9.92$K and $U = 29.4$ ms^{-1} at 0° latitude is at the high end of observed 3d UFKW amplitudes quoted in Gu et al. (2014), Liu et al. (2015) and England et al. (2012). We note that U peaks at an altitude of about 110 km, which is where exponential growth with height ceases, and molecular viscosity and thermal conductivity begin to determine the behavior of the UFKW. Below 110 km, the horizontal structure of U is characterized by the Gaussian shape of its corresponding Hough mode. Above this height the phase progression with height begins to measurably change with latitude, with longer λ_z occurring at higher latitudes. Also, the latitude structure of U flattens and spreads to higher latitudes with height, and assumes non-zero values at the poles. (This extension of UFKW wind amplitudes to the poles cannot occur for $s \neq -1$ UFKWs, since only wind oscillations with $|s| = 1$ can exist at the poles Hernandez et al. (1992, 1993).) The htvslat structure for ΔT similarly spreads latitudinally and develops longer λ_z at higher latitudes, although continuity at the poles requires zero amplitudes there. The horizontal structure of V develops maxima at the poles in the strongly dissipative regime above 150 km, an unusual characteristic for UFKW which are usually thought to be oscillations confined to low latitudes. These modifications to amp/phz structures are indicative of the inseparability of the system of equations in the dissipative thermosphere.

A theoretical basis for the vertical evolution of horizontal structures described above is provided in the analytic work of Volland (1974; see also Volland and Mayr, 1977) developed for solar tides, but which can reasonably be expected to apply to UFKW as well (e.g., Forbes, 2000). Volland (1974) approximates the molecular viscosity and thermal conductivity diffusion terms in the momentum and thermal energy equations with linear friction terms with coefficients that increase exponentially with height, and which enter as the imaginary part of a complex frequency, ω_c: ($\omega_c = \omega + i\nu_{eff}$). Volland (1974) then discusses the behavior of the solutions to the linearized equations with complex frequency as ν_{eff}/ω increases from ≤ 1 to $>> 1$, i.e., as z increases from ∼110 km to ∼200 km. In this dissipative regime, he shows that the Class I (gravity) and Class II (rotational) solutions to LTE pass over to a single 'thermospheric mode' of oscillation with eigenfunctions characteristic of gravitational modes but with negative eigenvalues, the latter traditionally being associated with evanescent solutions. Moreover, as ν_{eff}/ω becomes large, solutions approach U ∼ constant, V ∼ $\sin\theta$, and T ∼ $\cos\theta$, which characterize the salient features of the solutions above ∼200 km depicted in Figure 1. Further details can be found in Volland (1974), Volland and Mayr (1977) and Forbes (2000).

Another interesting feature of the structures in Figure 1 is the variation with height of the vertical wavelength (λ_z), as indicated by the spacing of the colored contours. The λ_z for U transitions from a λ_z of 71 km in the mesosphere (50 km to 80 km) to a λ_z of 51 km in the lower thermosphere (90 km to 120 km), and then to 165 km (463 km) at 150 km (200 km) altitude. (At these high altitudes the traditional definition of λ_z as the distance between two wave crests does not apply, and the quoted values are "equivalent" λ_z based on the rate of phase progression extrapolated to $2\pi/3d$. In classical tidal theory, which neglects the effects of dissipation, a quantity of the form $m^2 = [H(\kappa + dH/dz)/h_n - 1/4]/H^2$ appears in the vertical structure equation that suggests its interpretation as the square of a vertical wavenumber $m = 2\pi/\lambda_z$. This leads to the following expression for the vertical wavelength of a vertically-propagating oscillation:

$$\lambda_z \approx \frac{2\pi H}{\sqrt{\frac{H}{h_n}(\kappa + \frac{dH}{dz}) - \frac{1}{4}}} \tag{2}$$

where H is the scale height of the background atmosphere, $\kappa = R/c_p$, and h_n is the so-called "equivalent depth" (eigenvalue) of the associated Hough mode. Taking mesospheric values of $H = 6.78$ Km and $dH/dz =$ -.073 and $h_n = 2.23$ km, equation (2) yields $\lambda_z =$ 67 km, in reasonable agreement with the HME value of 71 km noted above. For lower thermosphere values of $H = 6.00$ Km and $dH/dz = +.20$, a value of $\lambda_z = 37$ km is obtained, in contrast to the HME value of 51 km. However, equation (2) neglects the effects of dissipation, the presence of which in the HME likely accounts for much of this disparity. At the very least, equation (2) appears to account for the shift from longer λ_z to shorter λ_z below/above the mesopause as indicated in Figure 1. At higher altitudes where molecular dissipation is even more influential, λ_z lengthens and approaches ∞ as amplitudes and phases asymptote to constant values in the upper thermosphere.

Figure 2 presents U amps/phzs for the 2d and 4d UFKWs for F10.7 = 75, with mesospheric λ_z of 244 km and 46 km, respectively. These λ_z transition to 81 km and 41 km, respectively in the lower thermosphere, before increasing with height at higher levels. The latitudinal width of the 2d UFKW is wider than that of the 4d UFKW, consistent with expectations from inviscid classical wave theory. The 2d UFKW in Figure 2 achieves a maximum amplitude of 68 ms^{-1} at an altitude of 111 km, and effectively penetrates to higher levels ($\sim$ 15 ms^{-1} at 250 km). To the contrary, the 4d(5d) UFKWs only achieve maximum amplitudes of 33(28) ms^{-1} at 104 km and amplitudes of 3(1.5) ms^{-1} at 250 km. These differences can be understood by estimating the relative importance of viscous(thermal conductivity) terms to $\partial/\partial t$ terms in the UFKW momentum(thermal energy) equations. For molecular viscosity, this ratio is

$$\chi = \frac{4\pi^2}{\lambda_z^2}\frac{\mu_0}{\rho_0 \delta\Omega} \tag{3}$$

where λ_z is the vertical wavelength; μ_0 is the coefficient of molecular viscosity; ρ_0 is the total mass density, which increases with level of solar activity; and $\delta\Omega$ is the wave frequency, where $\delta = 0.5(0.2)$ for 2d(5d) UFKW. For a Prandtl number of unity, a similar condition holds for the thermal energy equation (Forbes and Garrett, 1979). According to expression (3), at a given height the effects of viscosity are greatest for waves with smaller λ_z, smaller δ and smaller ρ_0, consistent with results discussed connection with Figures 1 and 2. The dependence on the square of λ_z is also notable.

To summarize, as UFKW periods(frequencies) progressively increase(decrease) from 2d(0.5d^{-1}) to 5d(0.2d^{-1}), their latitudinal extents progressively increase while their λ_z entering the thermosphere progressively decrease from 244 km to 37 km. According to (3), molecular dissipation is inversely proportional to both the wave frequency and the square of λ_z. Therefore, UFKW with the longer periods are severely dissipated, their vertical penetration severely curtailed, and their amplitudes reduced, compared to those with shorter periods. In our numerical model, it is our experience that diurnal tides ($\delta = 1.0$) with $\lambda_z < 30$ km do not penetrate efficiently into the thermosphere. This explains why the $s = -1$ 2d-5d first *antisymmetric* propagating modes with $\lambda_z \leq 15$ km are not considered in the present study. The same applies to UFKWs with periods > 5d which possess mesospheric $\lambda_z \leq 37$ km.

4.2 Dependence on solar activity level

In this section we investigate the dependence of UFKWs on solar cycle, with focus on the 3d UFKW. The role of ion drag in determining the vertical penetration and solar cycle dependence of the 3d UFKW is also examined. For this purpose HMEs were calculated for F10.7 levels of 75 through 200 in increments of 25 s.f.u. All the numerical values are consistent with the same normalizations as Figures 1 and 2; that is, a maximum (equatorial) temperature of 10K at 98 km for F10.7 = 75. Moreover, while $U, \Delta T$ and $\Delta\rho/\rho_0$ are perhaps the more physically relevant quantities in terms of comparisons with observations and so forth, here we consider $U, W, \Delta T/T_0$ and $\Delta\rho/\rho_0$ since these are the quantities whose physical inter-relationships primarily determine the behavior of the HMEs. For instance, if we omit the terms in the linear perturbation equations delineated in Forbes (1982) that relate to a latitudinally-varying background atmospheric state, then the following forms of the continuity, thermal energy, zonal momentum equation, and state equations, respectively, in the thermosphere relate $u', w', T'/T_0, \rho'/\rho_0$ (the time domain analogs of $U, W, \Delta T/T_0$ and $\Delta\rho/\rho_0$):

$$\frac{\partial}{\partial t}(\frac{\rho'}{\rho_0}) = -w'\frac{1}{\rho_0}\frac{d\rho_0}{dz} - \chi' \tag{4}$$

$$\frac{\partial}{\partial t}(\frac{T'}{T_0}) = -w'\frac{1}{T_0}\frac{dT_0}{dz} - (\gamma - 1)\chi' + F_\kappa T' \tag{5}$$

$$\frac{\partial}{\partial t}u' + 2\Omega\cos\theta v' = -\frac{RT_0}{a\sin\theta}\frac{\partial}{\partial\lambda}\frac{p'}{p_0} - \epsilon_0 u' + F_\mu u' \tag{6}$$

$$\frac{p'}{p_0} = \frac{\rho'}{\rho_0} + \frac{T'}{T_0} \tag{7}$$

where θ is colatitude, a is Earth's radius, R is the gas constant, $\gamma = c_p/c_v$, χ' is the divergence of the perturbation velocity field, subscript zeroes represent the zonal- and diurnal-mean averaged basic state (a function of height only), and the primes represent perturbations on that basic state. The quantities

$$F_\mu = \frac{1}{\rho_0}\frac{\partial}{\partial z}\mu_0\frac{\partial}{\partial z}, \ F_\kappa = \frac{\gamma - 1}{R\rho_0}\frac{\partial}{\partial z}\kappa_0\frac{\partial}{\partial z} \tag{8}$$

represent the effects of molecular viscosity and thermal conductivity, respectively. The UFKW fields plotted in the figures in this paper represent amplitudes and phases of assumed complex solutions of the primed quantities in the above equations of the form $e^{i(\sigma t + s\lambda)}$.

The reader is first referred to Figure 3(a), where the solar cycle variations of U and $\Delta T/T_0$ at 400 km altitude are plotted. All values are normalized to a value of unity at F10.7 = 75, and the normalization factors are provided below the figure. The figure shows that U = 8.7 ms^{-1} at F10.7 = 75, and reduces to 0.40 times this value for F10.7 = 200. On the other hand, $\Delta T/T_0$ = 1.16% (ΔT = 8.7K) at F10.7 = 75 and decreases to 0.68 times this value for F10.7 = 200. Moreover, when the ion drag coefficients ($\epsilon_0, \epsilon_0 \sin^2 I$, where I is the magnetic dip angle) in the zonal and meridional momentum equations are set equal to zero ($\epsilon_0 = 0$), the U and $\Delta T/T_0$ amplitudes at F10.7 = 75 increase to 28.2 ms^{-1} and 2.46% (ΔT = 18.5K) with modest changes in the variation with respect to solar cycle. Notable results of these numerical experiments thus include the smaller variation with solar cycle of $\Delta T/T_0$ compared to U; and the influence of ion drag, which serves to reduce $\Delta T/T_0$ by a factor of ∼2 and U by a factor of ∼3-4, depending on level of solar activity, from their $\epsilon_0 = 0$ values.

Height profiles of U and $\Delta T/T_0$ are presented in Figures 3(d) and 3(e), respectively, for F10.7 = 75 and F10.7 = 175. In Figure 3(d), we see the influences of molecular dissipation alone in the $\epsilon_0 = 0$ vertical profiles of U: the profiles reach a peak near 110 km, and then decrease by about a factor of 2 before increasing slightly and then asymptoting to constant values at higher altitudes. This type of behavior was anticipated in early analytical work on atmospheric tides by Lindzen (1968), Yanowitch (1967) and Richmond (1975) (see also summary provided in Forbes and Garrett, 1979) wherein it was shown (i) that the peak height is influenced by the altitude where $\chi = 1$, and by the presence of rotation; and that (ii) the shape of the profile above the peak is determined by the quantity $\beta = 2\pi H_D/\lambda_z$, where H_D is the scale height for increase in dissipation. Specifically, as β increases, the more the wave amplitudes above the peak are expected to decrease prior to asymptoting to a constant value in the upper thermosphere. Since the vertical wavelengths of UFKW considered here are in the same range as those investigated in these early works, the same tendencies are expected to apply. In the present 3d UFKW case where the inviscid λ_z is fixed at about 71 km, the greater decrease in U amplitude above the peak for $\epsilon = 0$ and F10.7 = 175 (compared to U for $\epsilon = 0$ and F10.7

= 75 in Figure 3(d)) is qualitatively consistent with the fact that H_D increases with increased solar activity.

The analytic solutions referred to above were achieved by parameterizing the effects of molecular diffusion (e.g., expressions (8)) with an exponentially-increasing linear damping coefficient in the thermal energy equation, and thus are at best qualitatively relevant to the current results. Moreover, the predicted behavior with respect to β was obtained in connection with solution of the parameter y_n to the vertical structure equation in classical tidal theory, and the vertical structures of $U, W, \Delta T, \Delta\rho$ and Δp are all somewhat different (although not explicitly shown in those works) due to the different functional dependencies of these variables on y_n. The different vertical structures of U, $\Delta T/T_0$ and $\Delta\rho/\rho_0$ reflected in Figures 3(d)-3(f) should perhaps not be surprising in light of their different dependencies on y_n. The equatorial amp/phz vertical structures of all the variables referred to in Figure 3 ($U, W, \Delta T/T_0, \Delta T$ and $\Delta\rho/\rho_0$), for F10.7 = 75 and F10.7 = 175, and for $\epsilon_0 = 0$ and $\epsilon_0 \neq 0$, appear in Figure S4 of the SI.

We return now to the specific influence of ion drag on the solar cycle variability of $U, W, \Delta T/T_0, \Delta T$ and $\Delta\rho/\rho_0$. Since ion drag occurs in the momentum equations, with the predominant effect occurring with respect to U for the UFKW (e.g., equation (6)), we begin with the zonal wind, U. As indicated in Figure 3(a), the addition of ion drag reduces the magnitude of U in comparison to its $\epsilon_0 = 0$ value, and intensifies its decrease with increasing F10.7. However, this solar cycle variation is not monotonic with respect to F10.7 at all altitudes, as illustrated in Figure 3(c). There we note that the value of U at 250 km, U_{250}, decreases from F10.7 = 75 to 125, but then increases from F10.7 = 125 to 200. This is related to the steady increase in height of the F-layer maximum with increasing solar cycle (see Figure S3 in SI), which manifests as an increase(decrease) in ϵ_0(U) between F10.7 = 75 to 125, and a decrease(increase) in ϵ_0(U) from F10.7 = 125 to 200. This sensitivity underscores the direct influence of level of solar activity on the UFKW zonal wind exerted by the ion drag coefficient ϵ_0.

As illustrated in Figure 3(b), the overall reduction in U compared with $\epsilon = 0$ (Figure 3(d)), and the monotonic decrease of U with increasing solar cycle due to ion drag (Figures 3(a) and 3(c)), results in similar reductions in vertical velocity W, which must also translate to the velocity divergence, χ'. In the context of Equation (4), reductions in w' and χ' with increasing F10.7 imply a similar reduction in $\Delta\rho/\rho_0$. Moreover, in the upper thermosphere where the scale height (H) is approximately constant with altitude, the coefficient of w' reduces to 1/H, and since H increases with F10.7, this compounds the reduction in $\Delta\rho/\rho_0$ with respect to F10.7 as compared with w' acting alone. In contrast, in equation (6) the coefficient of w' involving the vertical gradient of background temperature tends to zero in the upper thermosphere, and the coefficient $\gamma - 1$ of χ' is 0.4 as compared to 1.0 in equation (4). These factors indicate that the reduction of $\Delta T/T_0$ with respect to increasing F10.7 (Figure 3(a)) should be more muted than that of $\Delta\rho/\rho_0$ (Figure 3(b)), and this is indeed the case. In addition, the presence of the F_κ term in equation (5), the effect of which is to remove vertical gradients in ΔT in the upper thermosphere, is clearly responsible for the differences in vertical structure between $\Delta T/T_0$ and $\Delta\rho/\rho_0$ reflected in Figures 3(e) and 3(f).

As a final point, we note the appearance of p'/p_0 in equation (6) and its relation to ρ'/ρ_0 and T'/T_0 in equation (7). From Figure S4 in the SI, it is noted that $\Delta\rho/\rho_0$ and $\Delta T/T_0$ are nearly in phase in the upper thermosphere, and thus both act in concert with each other and with U in terms of solar cycle variabilities displayed in Figures 3(a)-3(c).

4.3 Discussion of mean wind effects on UFKW HMEs and their use

Given that the calculation of HMEs omits background winds, and considering that UFKW possess longer periods than solar tides, the question arises as to what effects this omission might have on addressing the science questions raised in the Introduction that define the objectives of this paper, and on how HMEs might be employed in practice. In this subsection we provide and interpret results from numerical models in light of available measurements of zonal- and diurnal-mean winds ($\overline{U}$), leading to some new insights into how $\overline{U}$ are expected to influence the vertical propagation of UFKWs in the thermosphere. The subsection concludes with an assessment of the $\overline{U} = 0$ assumption on the conclusions of our study, and how this assumption potentially impacts the application of HMEs in scientific studies.

The potential influence of $\overline{U}$ on tides, UFKWs and planetary waves is often assessed in terms of the ratio of the wave's zonal phase speed (C_{ph}) to $\overline{U}$, although sufficiently large meridional gradients in $\overline{U}$ can also play a role (e.g., McLandress, 2002). C_{ph} is given by $\frac{-2\pi a \cos\theta}{sP}$ where P is the wave period in days. Therefore, as a point of reference, C_{ph} for the 3d UFKW with s = -1 is equal to that of the diurnal tide with s = -3 (DE3, also an UFKW), or 154 ms^{-1} at the equator. Gasperini et al. (2017) diagnose the effects of mean winds and dissipation on both DE3 and the 3d UFKW in a general circulation model for solar minimum conditions, and find that the effects of asymmetric mean winds are to distort the horizontal shapes of these waves, and to shift their centroids towards westward wind regimes.

A signature feature of the asymmetric winds depicted in Gasperini et al. (2017) are the $\sim \pm$40-60 ms^{-1} eastward(westward) jets between the equator and about 60° latitude in the summer(winter) hemisphere, with maxima between about 100 and 120 km. These jets are actually "secondary" jets that result from the deposition of momentum by eastward-(westward-) propagating GWs in the summer(winter) hemisphere that do not encounter critical levels in the westward(eastward) jets below that encompass both the stratosphere and mesosphere. However, in comparison with $\overline{U}$ distributions in the 100 km to 120 km height region between 40°S and 40°N latitude based on Wind Imaging Interferometer (WINDII) measurements from the Upper Atmosphere Research Satellite (UARS) (Zhang et al., 2007), these jets are much larger in magnitude than the typical 10 to 20 ms^{-1} $\overline{U}$ indicated by WINDII. Also, the secondary jets in WINDII $\overline{U}$ have their maxima at about 95 km, as opposed to ~110 km in Gasperini et al. (2017). Moreover, influence of these secondary jets on the $\overline{U}$ distributions in Gasperini et al. (2017) appears to extend up to ~150 km and perhaps beyond, especially for December solstice. Therefore, any distortions seen in DE3 or UFKW shapes due to $\overline{U}$ above ~100 km in Gasperini et al. (2017) represent exaggerations of what exists in reality.

However, the Gasperini et al. (2017) results are still useful for gaining new insights into the effects of asymmetric mean wind fields on UFKW. In particular, it is notable that these effects are significantly more severe for DE3 than for the UFKW despite the fact that they share the same C_{ph}, and that their full latitudinal widths at half-maximum are both about 30°, and thus are exposed to the same mean wind distributions. If we assume that to first order the above asymmetries in DE3 and the UFKW are accommodated by the linear superposition of one or more antisymmetric modes that are generated by "mode coupling" (e.g., Lindzen and Hong, 1974) or "cross coupling" Walterscheid and Venkateswaran (1979a,b), then this disparity between mean wind effects on DE3 and the UFKW can be plausibly explained as follows. The first antisymmetric mode of DE3 has horizontal structure similar in extent to the first symmetric mode and λ_z = 30 km, whereas the first antisymmetric mode of the UFKW has horizontal structure that is more equatorially confined than that of DE3 and with $\lambda_z = 7$ km (see Gasperini et al., 2017, their Figure 4). (Note: the higher-order modes of DE3 and 3d UFKW have even shorter λ_z, and likely play secondary roles.) Our interpretation is that relative to DE3, the UFKW is constrained in terms of its ability to distort in response to an asymmetric wind field through coupling into an antisymmetric mode, and moreover, that antisymmetric mode once generated is subject to about 18 times more dissipation than the antisymmetric mode of DE3. Note that any antisymmetric modes that result from the presence of mean winds have short λ_z, and cannot propagate vertically in the dissipative thermosphere. Therefore, their effects on distorting UFKWs are expected to remain local, a conclusion drawn in an earlier numerical study by Forbes (2000).

The work by Forbes (2000) is one that is specifically directed at assessing mean wind effects on the 3d UFKW. The numerical model that is employed is the same one used here to create HMEs, except that the background temperature, density and wind specifications are based on earlier-era models (Hedin, 1991; Hedin et al., 1996) for July and F10.7 = 90 s.f.u. The "realistic" $\overline{U}$ distribution adopted in that study is provided in Figure 4(a). Of particular relevance, the -12 ms^{-1} to +24 ms^{-1} $\overline{U}$ winds between 90 and 120 km are characterized by similar $\pm$wind magnitudes, and meridional and vertical gradients, to those reported by Zhang et al. (2007) during June, July and August. The $\overline{U}$ between 120 km to 250 km is currently unknown, due to the absence if both day and night wind measurements. However, the $\overline{U}$ in Figure 4(a) above 150 km is mainly attached to the in-situ solar-driven circulation, and is not open to the degree of uncertainty in $\overline{U}$ at lower altitudes that is thought to be mainly driven by dissipation of the full spectrum of waves propagating into the thermosphere from below.

Figure 4(b) depicts zonal wind amplitudes for the 3d UFKW based on the $\overline{U}$ winds in Figure 4(a), and Figure 4(c) shows the zonal wind amplitudes when $\overline{U} = 0$ above 88 km (corrected from 90 km as stated in Forbes, 2000). The tropospheric forcing is identical in both cases, with the horizontal shape given by the Hough function for the first symmetric (Kelvin) mode with period = 3d and s = -1. Comparing the two, the height-latitude structures and amplitudes are, as expected, identical below about 90 km. In Figure 4(b), there is only modest distortion compared to Figure 4(c) below 150 km, and above 150 km a nearly symmetric latitudinal shape emerges. This is consistent with the interpretation that the higher-order modes generated through mode coupling remain trapped near their levels of excitation. In Figure 4(c) the greater symmetry near the peak in the absence of mean winds is evident. With the addition of mean winds in Figure 4(b), the UFKW amplitude emerges above 150 km with a somewhat reduced amplitude compared with the no-wind case, presumably because the UFKW has passed over some of its energy to higher-order modes, which remain trapped at lower heights. In Figure 4(b) it is also noted that above 150 km the latitudinal structure remains symmetric, despite the presence of ± 24 ms^{-1} $\overline{U}$ winds in the equatorial region; presumably this is due to the dominant effects of dissipation.

The Forbes et al. (2000) study is confined to July conditions and the 3d UFKW. For other months of the year, the WINDII $\overline{U}$ observations remain within the $\pm$10-25 ms^{-1} range between 100-120 km, so significant differences in the degree of $\overline{U}$ effects on the 3d UFKW are not expected to occur throughout the year. The C_{ph} of the 2d(5d) UFKW is 1.5(0.6) times faster(slower) than the 3d UFKW, so one might expect mean wind effects on the 2d(5d) UFKW to be somewhat less(greater) than that of the 3d UFKW. On the other hand, the latitudinal half-width of the 2d(5d) UFKW is about 60(40)°, and the first antisymmetric mode of the 2d(5d) UFKW has a λ_z of 15(3) km. Based on the reasoning derived from the analysis of DE3 and the 3d UFKW results in Gasperini et al. (2017), it could be heuristically argued that inhibition of UFKW distortion in connection with mode coupling acts in opposition to the C_{ph} effect; that is, the 2d(5d) UFKW is more(less) subject to distortion through mode coupling than the 3d UFKW. However, this reasoning would benefit from a series of numerical experiments directed at these specific questions.

Assuming that the interpretation of the Figure 4 results are correct, then this suggests that the transfer of energy to higher-order modes might introduce an effective damping effect on the symmetric part of the UFKW that is not included in any of the HMEs calculated here. That is, that the HME UFKW emerging at, say, 150 km could hypothetically be somewhat larger than the quasi-symmetric UFKW that would emerge from a 100 km to 150 km region containing a typical $\overline{U}$ distribution. However, based on the comparisons between Figures 4(b) and 4(c), this effect does not appear to impact the broad conclusions drawn in previous subsections regarding the other effects of dissipation on vertically-propagating UFKWs, including broadening latitude structures with increasing height; lengthening vertical wavelengths with increasing latitude; the dependence of vertical penetration on UFKW period and associated λ_z; and the influences of ion drag, including its dependence on solar activity and the underlying physics of how ion drag in the momentum equation manifests in temperature and density responses as a function solar activity.

When fitting UFKW HMEs to data that represent an $s = -1$ UFKW, e.g., in the upper mesosphere and/or lower thermosphere, it must be remembered that the HME will only project onto the symmetric part of that experimentally-determined UFKW, and the HME will extrapolate that symmetric component to various heights and latitudes. In such a context, it may or may not matter whether that extrapolation does not include any asymmetries or distortions that have their origins in mean winds. It depends on the problem at hand. For instance, if the application involves the dynamo generation of electric fields, then it is relevant to note that by analogy with DE3 as established by Jin et al. (2008), it is the component of U that is symmetric about the equator and in the vicinity of the peak in Hall conductivity near 106 km that is primarily responsible for the efficient generation of electric fields (see also Forbes, He et al., 2020, on this latter point). (Recall that V and amplitudes are small compared to U amplitudes for UFKW). The asymmetric part of the wind field primarily exerts its dynamo influence through the generation of field-aligned currents (Maeda, 1974). Therefore, wind effects that simply produce asymmetries about the equator may be inconsequential in terms of affecting the generation of electric fields, whereas mean winds that displace the centroid of the UFKW U distribution with respect to the equator can result in large reductions in the electric fields that an UFKW would otherwise generate. Proximity to the Hall conductivity peak also implies that UFKW over the full range of 2d-5d may be important for generating electric fields, even though only shortest-period UFKW are effective in penetrating well into the thermosphere. Finally, in the application wherein an HME is fit to an UFKW measured in the lower thermosphere for the purposes of specifying lower boundary conditions for TIEGCM-ICON (Maute, 2017), the vertical-latitudinal extrapolation provided by the HME is not needed, since TIEGCM-ICON will model that UFKW evolution self-consistently with its own background wind field and dissipation. Therefore, judicious and effective use of UFKW HMEs requires a firm understanding of the problem at hand, the nature of the HMEs being fit, and how the simplifying assumptions behind the calculation of HMEs influences any interpretations that are made on the HME extrapolations based on that fit.

5 Conclusions

The htvslat structures and solar cycle variability of winds, densities and temperatures associated with $s = -1$ UFKWs with periods between 2d and 5d are investigated through the use of HMEs analogous to those employed in the literature for diurnal and semidiurnal tides. The conclusions drawn are as follows:

1. UFKW with periods $\gtrsim$ 5d do not effectively penetrate $\gtrsim$ 100 km altitude due to increased dissipation accompanying increasingly short λ_z and long periods.
2. Dissipation broadens UFKW latitude structures with increasing height and lengthens vertical wavelengths with increasing latitude.
3. Ion drag significantly dampens UFKW amplitudes in the thermosphere, and reduces their amplitudes in concert with changes in background atmospheric conditions that result from increased solar activity. The direct effect of ion drag is to decelerate the zonal wind. This leads to suppression of vertical velocity and velocity divergence that in turn diminish perturbation temperature and density responses.
4. The 20 to 40 ms^{-1} 3d UFKW E-region wind amplitudes reported herein, which are calibrated against observations in the 90 km to 100 km region reported in the literature, are of similar magnitude to DE3 winds extracted from ICON observations (Forbes et al., 2021), and which were shown to be responsible for F-region equatorial vertical drifts and electron density variability of order $\pm$5-10 ms^{-1} and 25-35%, respectively. Similar ionospheric impacts are expected from UFKWs.
5. It was noted herein that UFKWs are episodic, and do not represent responses to the type of quasi-steady day-to-day forcing that characterizes solar tides. Based on UFKW simulations published by Chang et al. (2020), it was argued that the thermosphere response is fast enough, and the typical length of UFKW events long enough, that UFKWs arguably achieve steady-state conditions on a regular basis; thus, the salient features of their structures are reasonably emulated by HMEs.
6. The potential effects of background winds ($\overline{U}$) on UFKW propagation in the thermosphere is assessed herein, based on numerical model results and measurements of $\overline{U}$. It was concluded through a combination of theoretical reasoning, interpretation of DE3 and UFKW results in Gasperini et al. (2017), and a simulation with a "realistic" $\overline{U}$ distribution as compared with one wherein $\overline{U} = 0$ (Forbes, 2000),

that these effects are sufficiently modest that their omission in the calculation of HMEs does not detract from the broad conclusions itemized above. Nevertheless, the arguments presented herein regarding $\overline{U}$ could potentially benefit from a series of numerical simulations that supplement those in Forbes (2000), although the absence of any observational determinations of the $\overline{U}$ distribution between 120 km and 250 km would remain a limiting aspect of any results so produced.

7. The UFKW HMEs analyzed here are described in the Supporting Information and accessible through Forbes et al. (2022), and can be used for scientific studies similar to those that have been conducted using tidal HMEs, as outlined in the Introduction.

Users of HMEs are cautioned not to overestimate the capabilities of HMEs with expectations that some level of *detail* regarding their behavior in the thermosphere can be emulated. Any fits of HMEs to experimental determinations of UFKWs project only on to the components of those UFKWs that are symmetric about the equator, and any HME calibrated in this way will only characterize a symmetric UFKW at various heights and latitudes outside the fitting domain. Whether this is sufficient for the scientific problem at hand must be determined by the user. In fact, a major motivation for creation of the HME data set was to enable characterization of observation-based UFKW lower boundary conditions for TIEGCM-ICON, by analogy with its currently-designed use for forcing solar tides (Maute, 2017). In such a scenario an $s = -1$ UFKW of given period based on ICON wind and temperature measurements would be fit the with corresponding HME, thus providing pole-to-pole specifications of all of its dependent variables as a function of longitude and UT for input into TIEGCM-ICON. TIEGCM-ICON would then model the latitude-height and time evolution of the UFKW, taking full self-consistent account of mean winds, dissipation, ion drag and dynamo electric fields, and all of the corresponding ionospheric consequences. In such a scenario the height-latitude evolution of the UFKW as provided by the HME is no longer needed or relevant. It is expected that the degree of utility of UFKWs in scientific studies and their level of veracity will emerge through their use.

6 Data Availability Statement

The Hough Mode and Hough Mode Extension data sets pertinent to this paper can be found at https://doi.org/10.5281/zenodo.7144325 (Forbes et al., 2022). (note to JGR publications: activation pending JGR publication doi to be placed on Zenodo web site).

Acknowledgments

This work was supported under award AGS-1630177 from the National Science Foundation, and by the ICON mission, which is supported by NASA's Explorers Program through contracts NNG12FA45C and NNG12FA42I.

References

Chapman, S., & Lindzen, R.S. (1970). *Atmospheric Tides*, D. Reidel, Dordrecht, Holland.

Chang, L.C., Palo, S.E., Liu, H.-L., Fang, T.-W., & Lin, C.S. (2010). Response of the thermosphere and ionosphere to an ultra fast Kelvin wave. *Journal of Geophysical Research: Space Physics, 115*, A00G04. https://doi.org/10.1029/2010JA015453

Chiu, Y.T. (1975). An Improved Phenomenological Model of Ionospheric Density, *Journal of Atmospheric and Terrestrial Physics, 37*, 1563–1570, 1975.

Cullens, C.Y., Immel, T.J., Triplett, C.C. et al. (2020). Sensitivity study for ICON tidal analysis. *Progress in Earth and Planet Sciences, 7*, 18 (2020). https://doi.org/10.1186/s40645-020-00330-6

Davis, R.N., Chen, Y.-W., Miyahara, S. & Mitchell, N.J. (2012). The climatology, propagation and excitation of ultra-fast Kelvin waves as observed by meteor radar, Aura MLS, TRMM and in the Kyushu-GCM, *Atmospheric and Chemical Physics, 12*, 1865–1879. https://doi:10.5194/acp-12-1865-2012

Emmert, J. T., Drob, D. P., Picone, J. M., Siskind, D. E., Jones, M. Jr., Mlynczak, M. G., et al. (2020). NRLMSIS 2.0: A whole atmosphere empirical model of temperature and neutral species densities. *Earth and Space Science, 7*, e2020EA001321. https://doi.org/10.1029/2020EA001321

England, S.L., Liu, G., Zhou, Q., Immel, T.J., Kumar, K.K., & Ramkumar, G. (2012). On the signature of the quasi-3-day wave in the thermosphere during the January 2010 URSI World Day Campaign. *Journal of Geophysical*

Research: Space Physics, 117, A06304. https://doi.org/10.1029/2012JA017558

Flattery, T.W. (1967). Hough Functions. *Technical Report, No. 21*, Department of Geophysical Sciences, University of Chicago.

Forbes, J.M. (1982). Atmospheric tides. I. Model description and results for the solar diurnal component. *Journal of Geophysical Research: Space Physics, 87*, 5222–5240.

Forbes, J.M. (2000). Wave coupling between the lower and upper atmosphere: Case study of an ultra-fast Kelvin wave. *Journal of Atmospheric and Solar-Terrestrial Physics, 62*, 1603–1621.

Forbes, J.M., & Garrett, H.B. (1979). Theoretical studies of atmospheric tides. *Reviews of Geophysics, 17*, 1951–1981. https://doi.org/10.1029/RG017i008p01951

Forbes, J.M., & Vial, F. (1991). Semidiurnal tidal climatology of the E Region, *Journal of Geophysical Research: Space Physics, 96*, 1147–1157.

Forbes, J.M., & Hagan, M.E. (1982). Thermospheric extensions of the classical expansion functions for semidiurnal tides. *Journal of Geophysical Research: Space Physics, 87*, 5253–5259. https://doi.org/10.1029JA087iA07p05253

Forbes, J.M., Zhang, X., Palo, S.E., Russell, J., Mertens, C.J., & Mlynczak, M. (2009). Kelvin waves in stratosphere, mesosphere and lower thermosphere temperatures as observed by TIMED/SABER during 2002–2006. *Earth Planets Space, 61*, 447–453.

Forbes, J.M., Zhang, X., Hagan, M.E., England, S.L., Liu G., & Gasperini, F. (2017). On the Specification of Upward-Propagating Tides for ICON Science Investigations. *Space Science Reviews, 212*, 697–713. https://doi.org/10.1007/s11214-017-0401-5

Forbes, J.M., Maute, A., & Zhang, X. (2020). Dynamics and electrodynamics of an ultra-fast Kelvin wave (UFKW) packet in the ionosphere-thermosphere (IT). *Journal of Geophysical Research: Space Physics, 125*, e2020JA027856. https://doi.org/10.1029/2020JA027856

Forbes, J.M., He, M., Maute, A., & Zhang, X. (2020). Ultrafast Kelvin wave variations in the surface magnetic field. *Journal of Geophysical Research: Space Physics, 125*, e2020JA028488. https://doi.org/10.1029/2020JA028488

Forbes, J.M., Zhang, X., Heelis, R., Stoneback, R., Englert, C.R., Harlander, J.M., et al. (2021). Atmosphere-Ionosphere (A-I) coupling as viewed by

ICON: Day-to-day variability due to planetary wave (PW)-tide interactions. *Journal of Geophysical Research: Space Physics, 126*, e2020JA028927. https://doi.org/10.1029/2020JA028927

Forbes, J.M., Zhang, X., & Palo, S.E. (2022). Thermosphere Hough Mode Extensions (HMEs) for Ultra-Fast Kelvin Waves (UFKWs) [Data set]. https://doi.org/10.5281/zenodo.7144325

Gasperini, F., Forbes, J.M., and M.E. Hagan (2017). Wave coupling from the lower to the middle thermosphere: Effects of mean winds and dissipation. *J. Geophys. Res. Space Physics, 122*, 7781–7797, https://doi:10.1002/ 2017JA024317

Gu, S.-Y., Dou, X., Lei, J., Li, T., Luan, L., Wan, W., & J.M. Russell III (2014). Ionospheric response to the ultrafast Kelvin wave in the MLT region. *Journal of Geophysical Research: Space Physics, 119*, 1369–1380, https://doi.org/10.1002/2013JA019086

Häusler, K., Oberheide, J., Lühr, H. & Koppmann, R. (2012). The Geospace Response to Nonmigrating Tides. F.-J. Lübken (Ed.), *Climate and Weather of the Sun-Earth System (CAWSES): Highlights from a Priority Program*, F.-J. Lübken (Ed.), 481–506, Springer Atmospheric Sciences, New York. https://doi.org/10.1007/978-94-007-4348-9

Hedin, A.E., Fleming, E.L., Manson, A.H., Schmidlin, F.J., Avery, S.K., Clark, R.R., Franke, S.J., Fraser, G.J., Tsuda, T., Vial, F., & Vincent, R.A. (1996). Empirical wind model for the upper, middle and lower atmosphere. *Journal of Atmospheric and Terrestrial Physics, 58,* 1421–1448. https://doi.org/10.1016/0021-9169(95)00122-0

Hernandez, G., Smith, R.W., Fraser, G.J. & Jones, W.L. (1992). Large-scale waves in the upper mesosphere at Antarctic high latitudes, *Geophysical Research Letters, 19*, 1347–1350.

Hernandez, G., Fraser, G.J., & Smith, R.W. (1993). Mesospheric 12-hour oscillations near South Pole, Antarctica, *Geophysical Research Letters, 20*, 1787–1790.

Jin, H., Miyoshi, Y., Fujiwara, H., & Shinagawa, H. (2008). Electrodynamics of the formation of ionospheric wave number 4 longitudinal structure. *Journal of Geophysical Research, 113*, A09307. https://doi.org/10.1029/2008JA013301

Lindzen, R.S. (1968). Vertically propagating waves in an atmosphere with Newtonian cooling inversely proportional to density. *Canadian Journal of Physics,* *46*, 1835–1840. https://doi.org/10.1139/p68-520

Lindzen, R.S., & Hong, S.-S (1974). Effects of Mean Winds and Horizontal Temperature Gradients on Solar and Lunar Semidiurnal Tides in the Atmosphere. *Journal of Atmospheric Sciences, 31,* 1421–1446. https://doi.org/10.1175/1520-0469(1974)031¡1421:EOMWAH¿2.0.CO;2

Lindzen, R.S., Hong, S.-S., & Forbes, J.M. (1977). Semidiurnal Hough mode extensions in the thermosphere and their application. *Memorandum Report 3442*, Naval Research Laboratory, Washington, D.C.

Liu, G., England, S.L., Immel, T.J., Frey, H.U., Mannucci, A.J., & Mitchell, N.J. (2015). A comprehensive survey of atmospheric quasi 3 day planetary-scale waves and their impacts on the day-to-day variations of the equatorial ionosphere. *Journal of Geophysical Research: Space Physics, 120*, 2979–2992, https://doi.org/10.1002/2014JA020805

Liu, G., England, S.L., & Janches, D. (2019). Quasi two-, three-, and six-day planetary-scale wave oscillations in the upper atmosphere observed by TIMED/SABER over 17 years during 2002–2018. *Journal of Geophysical Research: Space Physics, 124,* 9462–9474. https://doi.org/10.1029/2019JA026918

Longuet-Higgins, M.S. (1968). The eigenfunctions of Laplace's tidal equations over a sphere. *Philosophical Transactions of the Royal Society of London. Series A, Mathematical and Physical Sciences, 262*, 511–607. http://www.jstor.org/stable/73582

Maeda, H. (1974). Field-aligned current induced by asymmetric dynamo action in the ionosphere. *Journal of Atmospheric and Solar-Terrestrial Physics, 36*, 1395–1401. https://doi.org/10.1016/0021-9169(74)90216-5

Maute, A. (2017). Thermosphere-Ionosphere-Electrodynamics General Circulation Model for the Ionospheric Connection Explorer: TIEGCM-ICON. *Space Science Review, 212*, 523–551. https://doi.org/10.1007/s11214-017-0330-3

McLandress, C. (2002). The seasonal variation of the propagating diurnal tide in the mesosphere and lower thermosphere: Part II. The role of tidal heating and zonal mean winds. *Journal of the Atmospheric Sciences, 59*, 907–922. https://doi.org/10.1175/1520-0469(2002)059¡0907:TSVOTP¿2.0.CO;2

Oberheide, J., Forbes, J.M., Häusler, K., Wu, Q., & Bruinsma, S.L. (2009). Tropospheric tides from 80 to 400 km: Propagation, interannual variability, and solar cycle effects.*Journal of Geophysical Research: Space Physics, 114*, D00I05. https://doi.org/10.1029/2009JD012388

Oberheide, J., Forbes, J.M., Zhang, X., & Bruinsma, S.L. (2011). Climatology of upward propagating diurnal and semidiurnal tides in the thermosphere. *Journal of Geophysical Research: Space Physics, 116*, A11306. https://doi.org/10.1029/2011JA016784

Pancheva, D., Mukhtarov, P., Siskind, D.E., & Smith, A.K. (2016). Global distribution and variability of quasi 2-day waves based on the NOGAPS-ALPHA reanalysis model. *Journal of Geophysical Research: Space Physics, 121*, 11,422–11,449. https://doi.org/10.1002/ 2016JA023381

Richmond, A.D. (1975). Energy relations of atmospheric tides and their significance to approximate methods of solution for tides with dissipative forces, *Journal of the Atmospheric Sciences, 32*, 980–987. https://doi.org/10.1175/1520-0469(1975)032¡0980:EROATA¿2.0.CO;2

Salby, M.L., Hartmann, D.L., Bailey, P.L., & Gille, J.C. (1984). Evidence for equatorial Kelvin modes in Nimbus-7 LIMS. *Journal of the Atmospheric Sciences, 41*, 220–235.

Svoboda, A.A., Forbes, J.M., & Miyahara, S. (2005). A space-based climatology of diurnal MLT tidal winds, temperatures and densities from UARS wind measurements. *Journal of Atmospheric and Solar-Terrestrial Physics, 67*, 1533–1543.

Volland, H. (1974). Solutions of Laplace's tidal equation for complex frequencies. *Journal of Atmospheric and Terrestrial Physics, 36,* 445–460. https://doi.org/10.1016/0021-9169(74)90125-1

Volland, H. (1988). Atmospheric Tidal and Planetary Waves. Kluwer, Dordrecht. pp. 348. https://doi.org/10.1007/978-94-009-2861-9

Volland, H., & Mayr, H.G. (1977). Theoretical aspects of tidal and planetary wave propagation at thermospheric heights. *Reviews of Geophysics and Space Physics 15,* 203–226. https://doi:10.1029/RG015i002p00203

Walterscheid, R. L., & Venkateswaran, S.V. (1979a). Influence of Mean Zonal Motion and Meridional Temperature Gradients on the Solar Semidiurnal Atmospheric Tide: A Spectral Study. Part I: Theory. *Journal of Atmospheric Sciences, 36*, 1623–1635. https://doi.org/10.1175/1520-

0469(1979)036¡1623:IOMZMA¿2.0.CO;2

Walterscheid, R. L., & Venkateswaran, S.V. (1979b). Influence of Mean Zonal Motion and Meridional Temperature Gradients on the Solar Semidiurnal Atmospheric Tide: A Spectral Study. Part II: Numerical Results. *Journal of Atmospheric Sciences, 36*, 1636–1662. https://doi.org/10.1175/1520-0469(1979)036¡1636:IOMZMA¿2.0.CO;2l

Yanowitch, M. (1967). Effect of viscosity on gravity waves and the upper boundary condition. *Journal of Fluid Mechanics, 29*, 209–231. https://doi.org/10.1017/S002211206700076X

Zhang, S.P., McLandress, C., & Shepherd, G.G. (2007). Satellite observations of mean winds and tides in the lower thermosphere: 2. Wind Imaging Interferometer monthly winds for 1992 and 1993. *Journal of Geophysical Research: Space Physics, 112,* D21105. https://doi:10.1029/2007JD008457

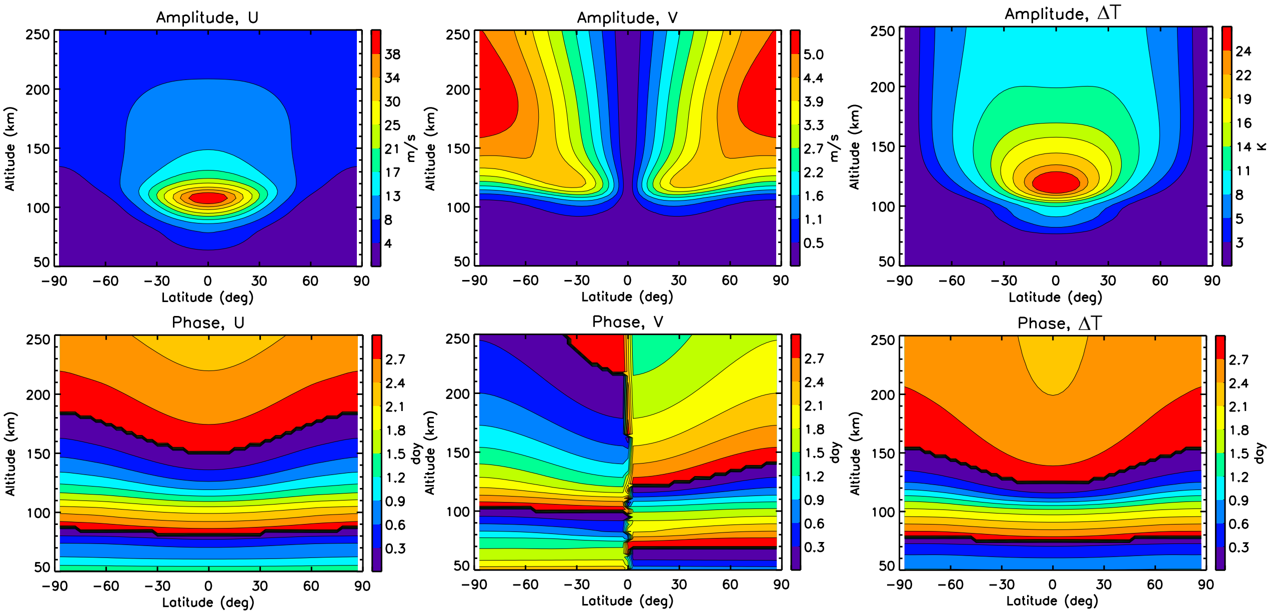

Figure 1. U, V, and ΔT amplitudes (top) and phases (middle) of the 3d UFKW for F10.7 = 125 as a function of height and latitude.

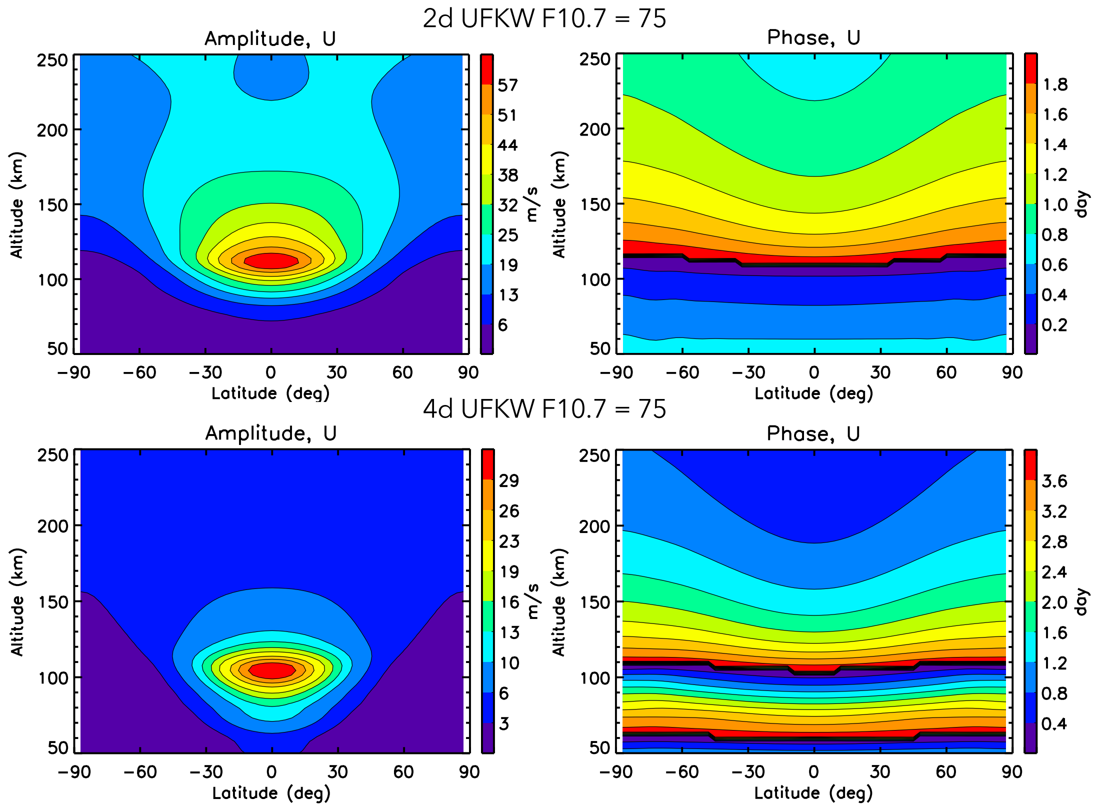

814 **Figure 2.** Amplitude (left) and phase (right) of U for 2d (top) and 4d (bottom) UFKW as a
815 function of height and latitude for F10.7 = 75.

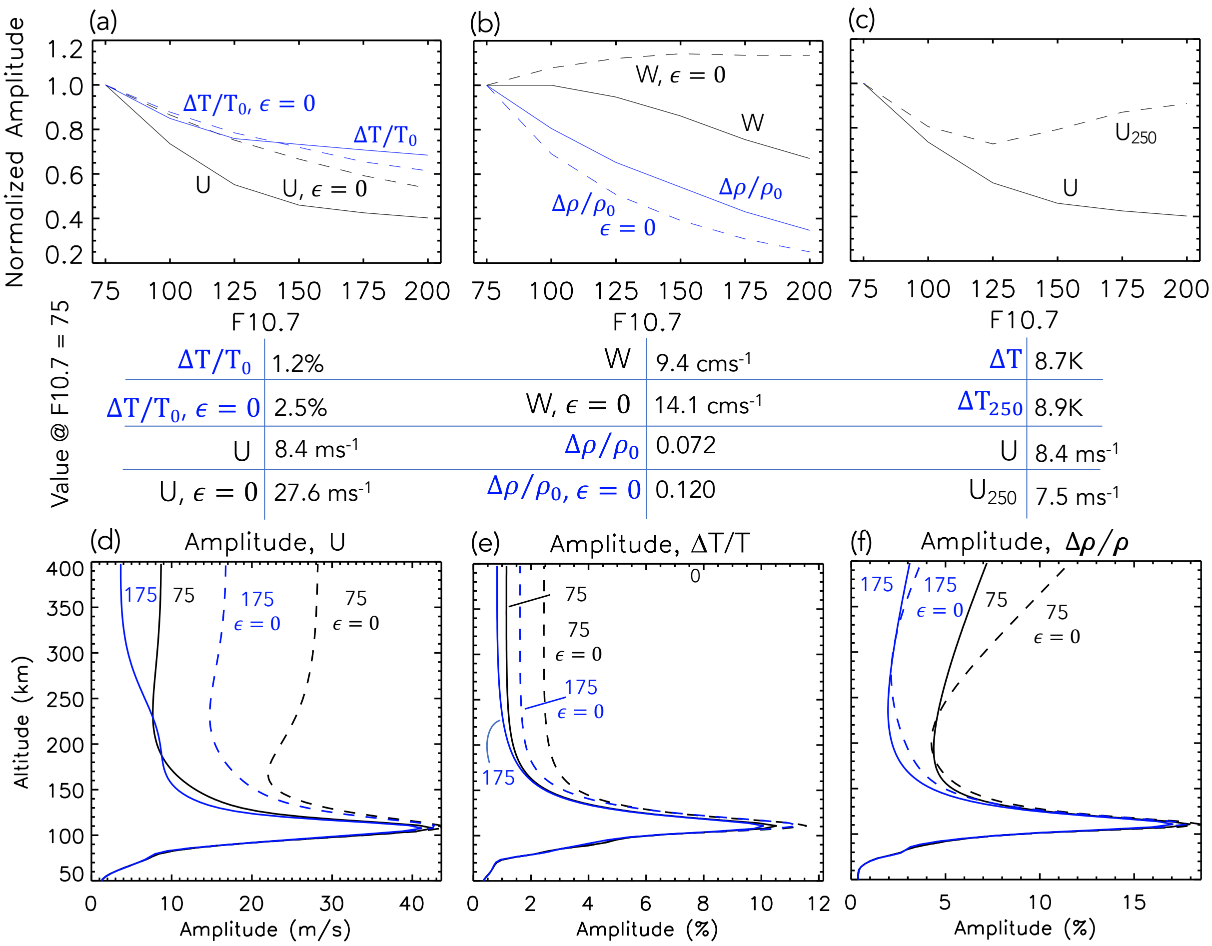

816 **Figure 3.** Panels (a) and (b): Latitude vs. F10.7 variability of various UFKW dependent
817 variables at 400 km altitude with and without ($\epsilon_0 = 0$) ion drag, normalized to unity at F10.7 =
818 75. Normalization factors are provided just below panels (a) and (b). Panel (c): Amplitude vs.
819 F10.7 variability of U at 400 km altitude and U at 250 km altitude (U_{250}), normalized to unity
820 at F10.7 = 75 according to the factors just below panel (c). Panels (d)-(f): height profiles of U,
821 $\Delta T/T_0$ and $\Delta\rho/\rho_0$, respectively, for F10.7 = 75 and F10.7 = 175 with and without ($\epsilon = 0$) ion
822 drag.

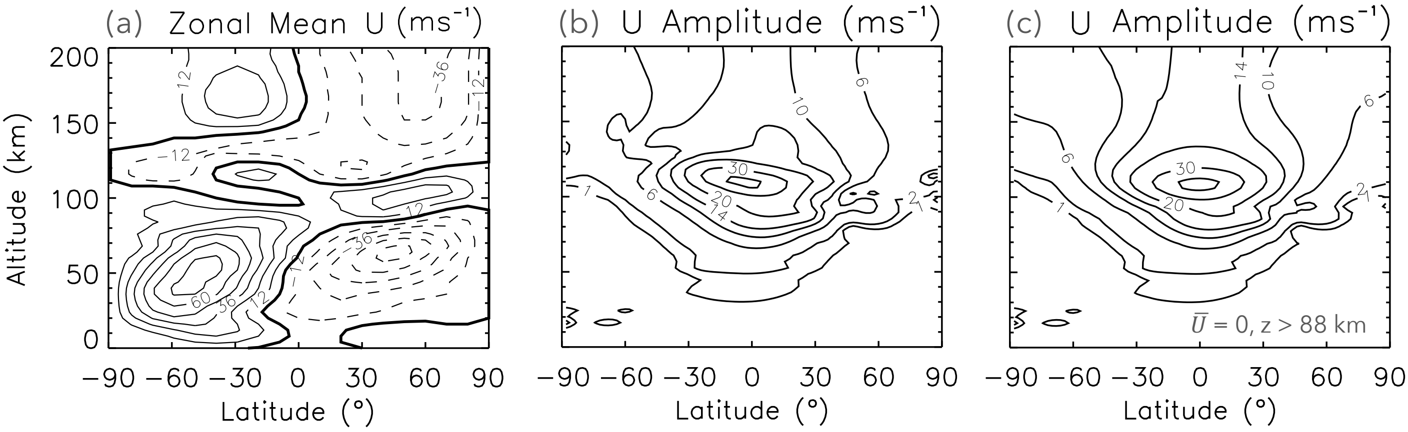

823 **Figure 4.** Results from numerical modeling of the 3d UFKW as described in Forbes (2000),
824 replotted here from 0 km to 200 km altitude: (a): $\overline{U}$ assumed in the calculations. (b): U ampli-
825 tude of the UFKW assuming the $\overline{U}$ distribution in (a). (c): The same as (b), except with $\overline{U} = 0$
826 for z > 88 km altitude. Panel (c) was not shown in Forbes (2000), which only illustrated results
827 for temperature and vertical velocity amplitudes for this particular numerical experiment.